RESEARCH PAPER

On the Importance of Direct-Levelling for Constitutive Material Model Calibration using Digital Image Correlation and Finite Element Model Updating

S. S. Fayad[1] · E. M. C. Jones[3] · D. T. Seidl[4] · P. L. Reu[3] · J. Lambros[2]

Abstract

Background Finite element model updating (FEMU) is an inverse technique that is used to identify material (constitutive) model parameters based on experimental data. These experimental data, often in the form of full-field strains, may be subject to a filtering bias unique to the measurement technique, which can propagate to material parameter identification error.

Objective Numerically adjusting for this filtering mismatch between the finite element analysis (FEA) and experimental measurements, here from Digital Image Correlation (DIC), is necessary to produce an accurate calibration. We investigate "direct-leveling" the FEA to the DIC data, i.e. computing strains using consistent methods and length scales for both data sets, before performing model calibration. Thus, both data sets have the same spatial resolution and can be quantitatively compared more readily.

Methods We generated two sets of synthetic "experimental" DIC displacement data: one directly from FEA nodal displacements and one from DIC images synthetically deformed according to the FEA displacements. We then explored how the FEMU material model parameter identification is affected by DIC user-defined settings, including virtual strain gauge size, step size, and subset shape function, as well as misalignment between the FEA and DIC datasets.

Results We found that direct-levelling of the FEA data before FEMU calibration returned more accurate results. This accuracy was independent of the DIC settings and spatial resolution. In contrast, performing FEMU with the unlevelled FEA data resulted in significant biases in the identified parameters.

Conclusion In FEMU-based calibrations, it is advantageous to properly level the strain from the FEA to match the filtering and spatial resolution of the DIC results.

Keywords Finite Element Model Updating · Digital Image Correlation · Virtual Strain Gage · DIC Levelling · Direct-Levelling

Introduction

With the increasing use of experimental full-field data as input for inverse material model calibration techniques [1], it is of interest to develop methodologies to improve model parameter identification accuracy. Full-field displacement and strain maps are usually obtained through optical techniques, one such popular method being digital image correlation (DIC). DIC, which contains both hardware and software components, can be affected by biases related to

✉ S. S. Fayad
  sfayad2@illinois.edu

  E. M. C. Jones
  emjones@sandia.gov

  D. T. Seidl
  dtseidl@sandia.gov

  P. L. Reu
  plreu@sandia.gov

  J. Lambros
  Lambros@illinois.edu

[1] Mechanical Science and Engineering, University of Illinois at Urbana-Champaign, Champaign 61801, USA

[2] Aerospace Engineering, University of Illinois at Urbana-Champaign, Champaign 61801, USA

[3] Diagnostic Science and Engineering, Sandia National Laboratories, Albuquerque, NM 87123, USA

[4] Scientific Machine Learning, Sandia National Laboratories, Albuquerque, NM 87123, USA

the processing algorithms and the experimental set-up. For the purposes of this work, which integrates DIC and finite element analysis (FEA), the bias errors can be separated into three groups:

1. Filtering errors such as subset shape function attenuation bias [2] and the similar but larger error of strain attenuation bias [3], as well as different strain formulations or calculation methods between DIC and FEA.
2. Image-induced errors such as pattern-induced bias (PIB) [4, 5], discrete truncation of grayscale values [4, 6], and image sampling errors such as subpixel interpolation bias [7].
3. Errors related to the physical experimental setup and hardware, such as image noise [8], heat haze [9–11], pattern delamination, and specimen fixturing issues.

The errors in group 3 are often hard to quantify and should be minimized at the experimental level if possible. The errors in group 2 are related to the images themselves and have been extensively studied for their effect on DIC measurements, e.g. [3–8, 12–14]. The errors in group 1 are related to the length scale and spatial resolution of the DIC displacement or strain measurements, which has been the topic of the recent DIC Challenge image sets [13, 14] and are the main focus of the present work.

Ideally, a DIC experiment is designed with sufficient spatial resolution such that deformation in regions of high gradients (i.e. in the necking region of a tensile dog bone or at strain concentrators like holes or notches) are adequately captured. However, in practical situations, this so-called strain convergence condition cannot always be guaranteed, and the DIC algorithms can be viewed as a low-pass filter that attenuates peak values of strains. The filtering effect is more pronounced for strains than displacements since the length scale for strains (the Virtual Strain Gauge (VSG)) is typically longer than that for displacements (the subset). Although displacements can be used as input to full-field calibration methods, often full-field strain maps are preferred as they are insensitive to rigid body motions and are assessed for model validation. Similarly, a FEA should also be designed to have sufficient spatial resolution to resolve strain gradients, which is accomplished through a mesh refinement study. Unlike DIC, which often has physical limitations for the best spatial resolution that can be achieved (e.g. camera detector size, lens optical resolution), the spatial resolution of FEA data can be improved with a finer mesh, limited only by computational time.

Discrepancies in length scale and spatial resolution between DIC and FEA data must be considered before quantitative strain error maps can be compared [15]. Lava et al.

[15] addressed this issue by proposing the "DIC-levelling" approach, where synthetic DIC images are created by deforming the reference experimental image according to the FEA nodal displacements. These images are then processed through the DIC software using the same user-defined settings as the experimental images. This so-called DIC-levelled FEA data conforms to the original FEA but has the same filtering and same spatial resolution as the experimental data, thus addressing group 1 errors. Additionally, group 2 image-based errors are also considered, since the same speckle pattern is used for both the experimental and DIC-levelled FEA data. The DIC-levelling approach is implemented in the commercial DIC software MatchID through the finite element (FE) Deformation and FE Validation modules [16] and has been applied for validation of an isotropic material model [17], an anisotropic material model [18], and a cased explosive [19]. Recently, DIC-levelling has been used to assess the contribution of the DIC error to the identification cost function [20].

While the effect of length scale and spatial resolution discrepancies was demonstrated for FE model validation, to the best of our knowledge DIC-levelling not been utilized for finite element model updating (FEMU) identification. Typically, FEMU using full-field motion data is performed by interpolating kinematic quantities such as the experimental displacements/strains onto the FE mesh (or vice-versa) and directly subtracting the two fields to measure the mismatch on a point-by-point basis. A residual, based on the weighted sum of squares of the deformation mismatch [21–25], is minimized with respect to the material model parameters in order to identify the best parameter set. Often kinetic values such as the global force is included in the cost function [23], but these measurements are not utilized in this paper for reasons discussed later. We show here that this "direct-subtraction" method with unlevelled kinematic FEA data can lead to biased calibration of the material model parameters. Similarly, other inverse calibration methods that employ full-field data, such as the Virtual Fields Method (VFM), can produce biased parameter results if the filtering effect of DIC is not considered [26–29]. This bias can be mitigated by judicious experimental design (i.e. avoiding sharp strain gradients) and careful selection of DIC parameters to optimize spatial resolution. However, assuring the DIC strains are converged is not always feasible.

The DIC-levelling method offers a path to address group 1 and group 2 errors with FEMU by rectifying discrepancies in spatial resolution before computing the cost function for calibration. However, we posit that the DIC errors in group 2 are often inconsequential in the model calibration process compared to the systemic biases in group 1. Therefore, here we have simplified the DIC-levelling process for FEMU to

capture only group 1 errors by calculating strains from FEA nodal displacements using the same polynomial shape functions as the experimental DIC measurements. This so-called "direct-levelling" process is more computationally efficient for FEMU than DIC-levelling since it bypasses generation and correlation of synthetic images at each iteration step of FEMU. Direct-levelling was first performed in [22], and later in [30] to handle the disparity in spatial resolution for the strain measurement, but has not been thoroughly investigated in the literature. We extend this procedure to also rectify filtering errors at the displacement (or subset) level before calculation of strain components.

The DIC-levelling and direct-levelling methods have both been developed in the context of local, subset-based DIC, where the user-defined DIC parameters (e.g. subset size, VSG size) are independent from the FEA parameters (e.g. element size). In contrast, global DIC [31, 32] and Integrated DIC (I-DIC) [23] offer alternatives to the levelling approach, since the experimental DIC analysis is conducted with the FEA mesh, inherently linking the spatial resolution of both data sets. However, I-DIC requires control of the DIC code and to the best of our knowledge has not been applied in stereo applications. Additionally, a majority of commercial DIC packages use local DIC, so the levelling approach is still necessary for a large number of FEMU cases.

This paper is organized as follows: In "Numerical Methods" we discuss construction of a finite element model of an hourglass specimen that generates heterogeneous, full-field strain data for FEMU. An isotropic elasto-plastic material model is employed with "ground-truth" parameter values based on tensile dog bone specimens of 304L stainless steel sheet metal. We then create two sets of synthetic "experimental" DIC data based on the deformation state of the FE model: in the first, strains are calculated directly from the FEA nodal displacements to isolate only group 1 errors; in the second, synthetic DIC images are generated and processed in DIC software to additionally incorporate group 2 errors. We then discuss the process of direct-levelling the FEA data to rectify identification error caused by the biases in DIC. Then in "Result and Descussion" we utilize direct-levelling to show that it is possible to perform FEMU with large VSG sizes and poor spatial resolution and obtain a unique and accurate set of material model parameters. We then performed FEMU with multiple DIC settings to better understand the effectiveness of direct-levelling and how the group 1 errors compare to that from group 2. Finally, we explore the effect of misalignment of the FE model to the DIC results on the identification and compare it to errors caused by filtering. In conclusion, we remark on the limitations of this method and ultimately recommend its use for material identification.

Numerical Methods

Finite Element Model and Constitutive Equations

A planar shell FE model with plane-stress conditions was made in ABAQUS 2020 Standard to represent the hourglass specimen geometry from [33], shown in Fig. 1(a). The mesh generated for the FEA along with an illustration of the boundary conditions are shown in Fig. 1(b). A magnified region of the middle section where plastic strain and strain gradients were largest is shown in Fig. 1(c). Displacement was constrained across the bottom surface in the y-direction only, and a uniform displacement of $V = 0.25$ mm was applied on the top surface in the y-direction. A single fixed point at the bottom left corner was added to constrain rigid body motions. Adaptive implicit time-stepping was used, with an initial displacement increment of 0.0025 mm and a maximum displacement increment of 0.025 mm. The FE model accounted for geometric and material nonlinearities and used the default ABAQUS convergence settings to solve the forward problem. Based on the symmetry of sample geometry and boundary conditions, a ¼ model could have been evaluated instead of the full geometry. However, in a physical experiment, small deviations from uniform and symmetric prescribed boundary conditions may occur, which can lead to a discrepancy with the FE model using idealized boundary conditions. To account for such variations, the experimentally measured displacement near the boundaries, such as motion measured by DIC, can be applied to the numerical model to achieve a more accurate representation of the experiment, as was done in [18]. For this reason, we opted to simulate the full model geometry to better transition our model and FEMU code for use with a physical experiment in a future study.
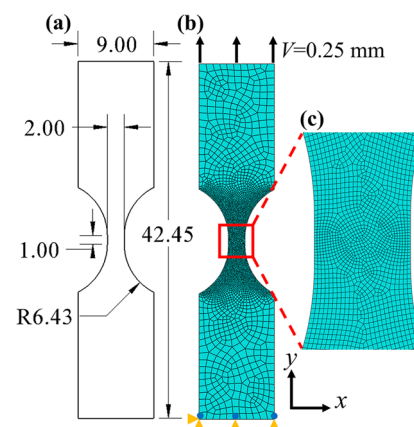

Fig. 1 Finite element model used in our experiment with (**a**) schematic of the specimen geometry (**b**) applied boundary conditions on our final 5202-element mesh with (**c**) a magnified view of the neck

Table 1 Row 1) Reference parameters used in the material model. Row 2) Initial guess of the material model parameters used in the finite element model. E, and ν were fixed while σ_0, B, and n were optimization variables

	Young's modulus, E (GPa)	Poisson's ratio, ν	Initial yield stress, σ_0 (MPa)	Hardening rate, B (MPa)	Hardening exponent, n
Reference	200	0.29	339	1,070	0.645
Initial Guess	N/A (fixed)	N/A (fixed)	305.1	1,177	0.5805

We used an isotropic elastoplastic material model with the flow stress, σ_y, based on a power law:

$$\sigma_y = \sigma_0 + B\left(\bar{\varepsilon}^p\right)^n \tag{1}$$

where σ_o is the initial yield stress, B is the hardening rate, n is the hardening exponent, and $\bar{\varepsilon}^p$ is the equivalent plastic strain, which is computed from the inelastic portion of the logarithmic strain in ABAQUS. In ABAQUS, this material model is implemented using the rate-independent Johnson–Cook model under isothermal conditions. The reference model parameters are shown in Table 1 and were based on experimental tensile tests which we conducted on three specimens cut from the transverse direction of a 304L stainless steel sheet material. In the current work, the elastic properties were fixed, and the plastic parameters were identified using FEMU, with the initial guess values chosen as $\pm 10\%$ of the reference value. The initial guess for σ_0 was chosen as the smaller value such that plasticity in the FEA

would be guaranteed for the first iteration of the FEMU procedure. Since the elastic parameters E and ν are fixed and assumed to be known, the global forces that result from the imposed displacements at the boundaries are not required in the FEMU optimization [23].

The bilinear, full-integration CPS4 element was used, and the mesh density was refined so the maximum logarithmic y-strain, ε_{yy}, converged to a final value as shown in Fig. 2. The N = 5,202 element mesh was chosen for its balance of spatial resolution (the maximum strain was within 0.03% of that from the mesh containing 18,456 elements) and computational efficiency. This mesh had a median element area of 0.0104 mm^2 and smallest element area of 0.0018 mm^2 at the neck (see Fig. 1(c).

The reference coordinates of the nodes and integration points, which were used to spatially register the FE mesh to the DIC image or point cloud, were obtained from the undeformed ABAQUS model at the initial time step. The
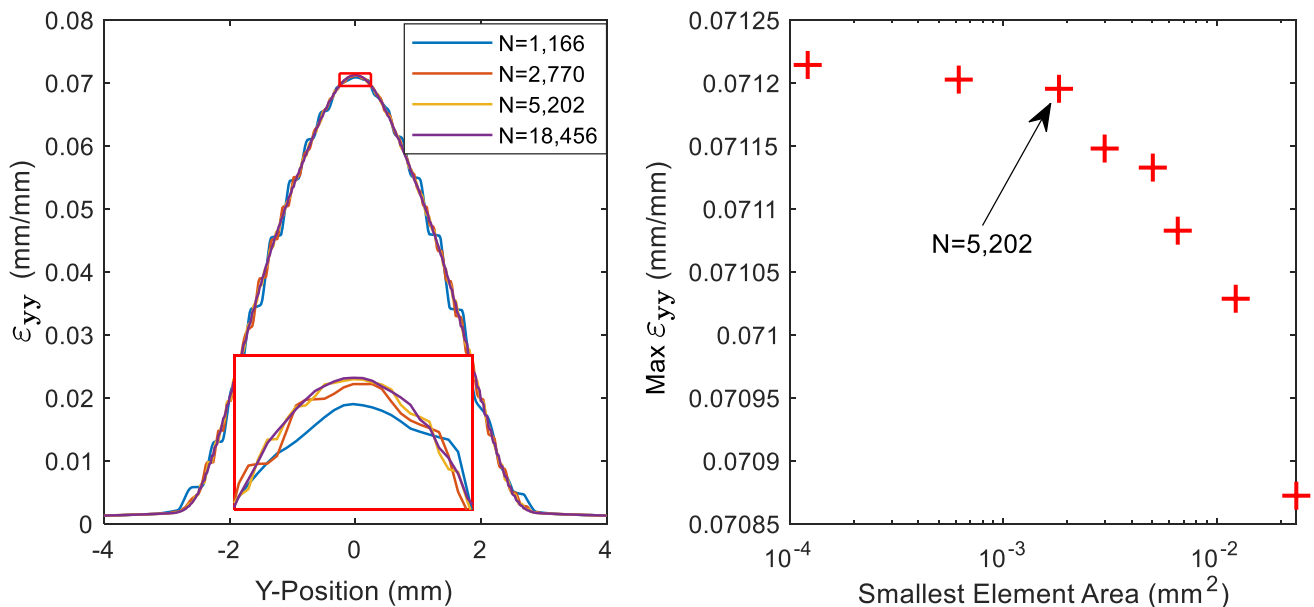

Fig. 2 Mesh convergence. Left: Line plot of the y-strain across the vertical centerline of the specimen with a magnified view of the peak strain in the inset. The mesh containing N = 5,202 elements was nearly indistinguishable from the finest mesh containing N = 18,456 elements, whereas the coarser meshes inadequately captured the strain across the peak. Right: Peak strain as a function of smallest element size used in the mesh. The chosen mesh containing N = 5,202 elements (shown in Fig. 1(b-c) had a peak strain within 0.03% of the finest mesh

kinematic quantities of displacement and strain were gathered from the FEA at the step where $V = 0.25$ mm.

Generation of "Experimental" Data

Two sets of synthetic "experimental" data were produced to evaluate the direct-levelling technique for FEMU. The first set was taken directly from the FEA nodal displacements in order to evaluate the identification error due to the group 1 problem of filtering bias. This data set isolates the strain attenuation bias and does not include effects of subset shape function attenuation bias nor any group 2 errors related to the DIC images. The second data set was taken from a pair of synthetic images generated from the FEA and processed in DIC software, to evaluate the effect of subset shape functions, DIC errors in group 2, and image noise on the identification.

Note that in reality, the true material response is rarely, if ever, exactly represented by an assumed analytical material model, resulting in a bias described as "material model form error" [15]. In this work, we utilized the same material model in the "experimental" data generation that we employed for the FE model used in our FEMU identification, thus eliminating the effects of material model form

error and instead allowing us to concentrate on the errors listed in the introduction. Including the effects of material model form error would obfuscate the effects of levelling on known DIC and experimental errors. However, though not considered in this work, understanding material model form error is an important topic that would be deserving of a separate study.

Synthetic "experimental" data set 1: Displacements taken directly from FEA

The first set of synthetic "experimental" data was created by interpolating the displacements from the FEA nodal locations onto a regular grid with a point-to-point spacing of 0.149 mm (equivalent to the DIC step size of 7 pixels used for the second set of synthetic "experimental" data in "Synthetic "experimental" data set 2: Displacements taken from synthetic DIC images". This was performed using MATLAB's triangulation-based cubic interpolation scheme. Next, the Green–Lagrange finite strain (a common strain tensor output from DIC codes) was computed in MATLAB using the polynomial shape function method described in "Strain Calculations for "Experimental" DIC Data").
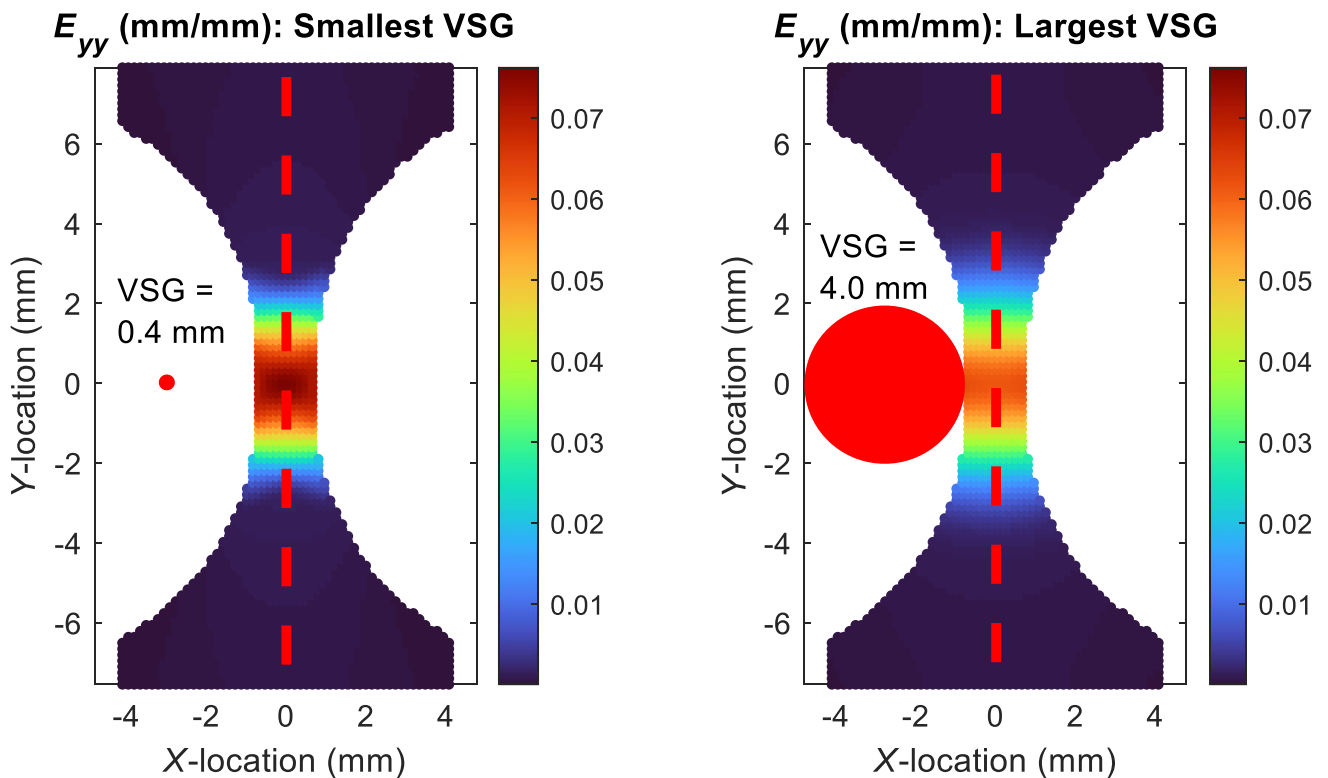

Fig. 3 Strain E_{yy} from the FE model analyzed using the reference parameter set along with its VSG for Left: the smallest VSG of 0.4 mm and Right: the largest VSG of 4.0 mm. The maximum resolved strain in the larger VSG is more than 0.015 (mm/mm) less than that of the smaller VSG as a result of the strain attenuation bias inherent to the polynomial strain calculation method
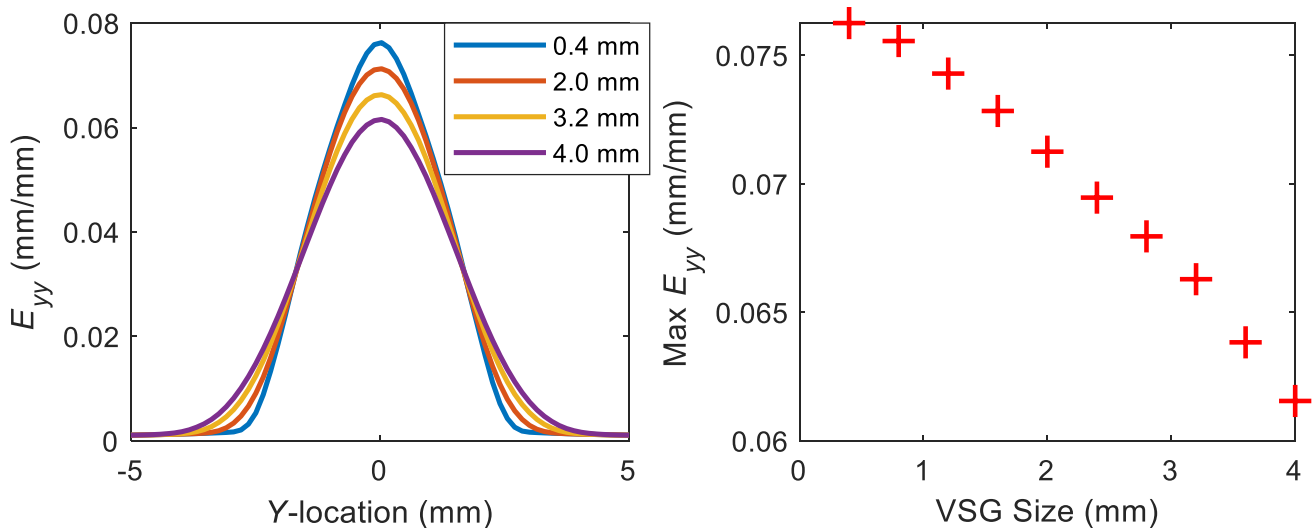
Fig. 4 Left: Line-cuts along the sample vertical centerline of the strain calculated from FEA displacement data differentiated over a VSG neighborhood. Only select VSGs are included for clarity. Right: The maximum E_{yy} obtained for each VSG size. The larger VSGs attenuate strain more and can ultimately cause a disparity between the experimental measure of strain and a higher resolution FEA-calculated strain

For this "experimental" data, 10 different virtual strain gage (VSG) sizes were used to obtain multiple levels of strain attenuation bias. The VSG sizes ranged from a small VSG of 0.4 mm to a, perhaps unreasonably, large VSG of 4.0 mm, in 0.4 mm increments. The VSG was defined as all points falling withing a circle with a diameter equal to the VSG size. A circular VSG, as opposed to a square VSG such as in [34], was used so the strain would only be influenced by points equidistant from the point of interest.

Figure 3 shows the vertical normal component, E_{yy}, of the full-field strain for the smallest and largest VSG. The color bar shows the strain results for the largest VSG size are filtered by over 0.015 mm/mm compared to the smallest VSG size. This strain attenuation bias can be more easily seen on the left plot in Fig. 4 via a line-cut across the center of the specimen (red dashes in Fig. 3). Additionally, the plot on the right of Fig. 4 shows the monotonic decrease in peak strain for the various VSG sizes. A 4.0 mm VSG may be unreasonable in practice, as the additional filtering can heavily alter the measured values of the strain. However, we will show in "Result and Discussion" that unique and accurate parameter identification via FEMU can still be performed with a VSG of this size.

Synthetic "experimental" data set 2: Displacements taken from synthetic DIC images

A second set of synthetic "experimental" data, based on synthetic DIC images, was generated to more closely resemble actual DIC data compared to Data Set 1. Synthetic

image generation and deformation was performed using the BSpeckleRender code described in [35], with specific settings outlined in Table S1 of the supplementary information. This code was chosen here since it does not use any interpolants to deform the image, as the accuracy of DIC can be obfuscated due to interaction between the image generation interpolant and the DIC interpolant [36, 37]. Therefore, the absence of an image interpolant lets us more accurately assess the effects of subpixel bias in the DIC analysis on the FEMU identification. Due to the high computational cost of this image generation code, only the central portion of the specimen was included in the computational domain, as this is the region that plastically deformed. Two undeformed-deformed image pairs were created, one without noise, and one with heteroscedastic noise added to each the reference and deformed image. The camera noise was based on a FLIR (formerly PointGrey) 5-Megapixel camera (GRAS-50S5C-C) and was the same noise model utilized in the DIC Challenge 2.0. [13]. The final image size was 900 pixels × 461 pixels with an image scale of 0.0212 mm/pixel. This resolution corresponded to an approximate stand-off distance of 180 mm, which was calculated using the equations provided in [38] by assuming a 25 mm lens and using the FLIR camera pixel size of 3.45 mμ. Figure 5(a) shows the resultant reference image created by the BSpeckleRender code.

DIC was performed using a subset size of 21 pixels, step of 7 pixels, and a normalized sum of square difference matching criterion. Two DIC codes were used in the analysis. The first, MatchID, allowed us to use a higher order quadratic shape function, but was restricted to a lower order
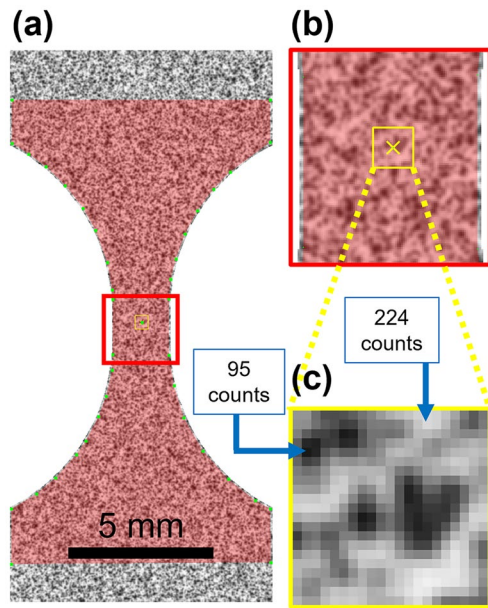
Fig. 5 (**a**) The reference image used in the analysis and ROI (red mask) which focused on the region where plastic deformation was likely to occur. (**b**) A zoomed in view of the neck of the specimen. (**c**) A representative subset/seed point of size 21 pixels used in the DIC analysis. A sample of the white background and black features show the pattern has roughly 130 counts of contrast with image gradients in both image directions

cubic spline image interpolant. The second, VIC2D, made use of the higher order 8-tap image interpolant, but was restricted to a lower order affine shape function. The original ROI was approximately the same in both codes, shown by the red mask in Fig. 5(a). The ROI was trimmed along the edges by 3–5 pixels (depending on the curvature of the hourglass specimen) such that the discretization of the border of the specimen in the image and any subsequent error caused by edge values [38] did not affect the DIC results. The initial seed point (Fig. 5(c) was the same in both codes so that points would be sampled at similar locations. A MATLAB routine was implemented to retain only points common to both data sets (2901 data points).

To obtain an intuitive sense of the best VSG size for the DIC analysis, we performed a VSG study [39] using the DIC results from the noisy images which would more closely replicate a physical experiment. By inspection, the strain converged to a final value of 0.075 mm/mm with a VSG size of approximately 0.8 mm before succumbing to noise at a VSG size of 0.4 mm. Therefore, we will designate the VSG size of 0.8 mm as our representative DIC result when comparing unlevelled and levelled FEMU identifications in "Result and Discussion").

Finite Element Model Updating

FEMU identifies the material model parameters by optimizing the similarity between experimental and FEA data for some quantity of interest, here the three in-plane strains, $\boldsymbol{\epsilon} = \langle \epsilon_{xx}, \epsilon_{yy}, \epsilon_{xy} \rangle$. To maintain a standard set of notations for the equations in the following sections, column vectors will be denoted by boldface (e.g. $\boldsymbol{\epsilon}$), and matrices will be denoted by boldface surrounded by brackets (e.g. $[\mathbf{H}]$). Optimization in FEMU is performed through:

$$\min_{\boldsymbol{\rho}} SSD \equiv \frac{1}{2} \sum_{\Omega_{exp}} \left(\boldsymbol{\epsilon}_{exp}(\boldsymbol{X}_{exp}) - \boldsymbol{\epsilon}_{FEA}(\boldsymbol{X}_{exp}, \boldsymbol{\rho}) \right)^T \\ \left(\boldsymbol{\epsilon}_{exp}(\boldsymbol{X}_{exp}) - \boldsymbol{\epsilon}_{FEA}(\boldsymbol{X}_{exp}, \boldsymbol{\rho}) \right), \quad (2)$$

which considers the unweighted sum-of-squared differences (SSD) between the three experimentally measured strain components, $\boldsymbol{\epsilon}_{exp}(\boldsymbol{X}_{exp})$, from the two cases of synthetic data described above, and the three strain components from the FEA $\boldsymbol{\epsilon}_{FEA}(\boldsymbol{X}_{exp}, \boldsymbol{\rho})$ across the experimental region of interest, Ω_{exp}, at individual measurement locations, $\boldsymbol{X}_{exp} \in \Omega_{exp}$. To keep the form of (2) general, the symbol $\boldsymbol{\epsilon}$ is used in (2) as opposed to the logarithmic strain, $\boldsymbol{\varepsilon}$, or Green–Lagrange strain, $\boldsymbol{E}$, specifically mentioned earlier. The experimentally measured strains depend on the strain tensor and accuracy of the measurement method, and the FEA strains depend on the material model parameter vector $\boldsymbol{\rho} = [\sigma_0, B, n; E, \nu]$, as well as any post-processing or levelling that is performed on the model output.

To solve the least-squares problem introduced in (2), the Gauss–Newton method was applied where the parameter vector was updated at each iteration of the optimization according to equations (3a, 3b, 3c) [23].

$$\delta \overline{\boldsymbol{\rho}}^{i+1} = [\mathbf{H}^i]^{-1} [\mathbf{S}^i]^T \left(\boldsymbol{\epsilon}_{exp} - \boldsymbol{\epsilon}_{FEA}(\boldsymbol{\rho}^i) \right), \quad (3a)$$

$$[\mathbf{H}^i] = [\mathbf{S}^i]^T [\mathbf{S}^i], \quad (3b)$$

$$[\mathbf{S}^i] = \left[\frac{\partial \boldsymbol{\epsilon}_{FEA}}{\partial \overline{\boldsymbol{\rho}}^i} \right]. \quad (3c)$$

The components of the parameter vector, $\boldsymbol{\rho}$, were divided by the initial guess to produce a normalized parameter vector, $\overline{\boldsymbol{\rho}}$, intended to improve performance of the optimization. The terms $\boldsymbol{\epsilon}_{exp}$, and $\boldsymbol{\epsilon}_{FEMU}$, without the specified location $\boldsymbol{X}$, represent the global strain vectors composed of the three in-plane strain components at all of the measurement points.

The FEA strain for the i'th iteration, $\epsilon_{FEA}(\boldsymbol{\rho}^i)$, was calculated using the current estimate of the material model parameters. The sensitivity matrix, $[\mathbf{S}]$, was calculated using a forward finite-difference approximation with a normalized parameter step size of 10^{-6} and required a separate forward solve for each parameter. As mentioned, the initial guess in Table 1 was carefully chosen so that $[\mathbf{S}]$ would be non-zero at the first FEMU iteration. We utilized the software ABAQUS2MATLAB [40] to communicate the FEA data from ABAQUS to our custom FEMU code in MATLAB. The optimization procedure required four separate forward solves and transcriptions of data from ABAQUS to MATLAB for each iteration to account for the current estimate of the strain and the finite difference perturbations for the three material parameters. The optimization ended when the convergence criterion, Φ, computed by the Euclidian norm of the parameter update, was less than 10^{-5} as shown in equation (4).

$$\Phi^{i+1} \equiv \|\delta\overline{\boldsymbol{\rho}}^{i+1}\| < 10^{-5}. \tag{4}$$

Strain Calculations for "Experimental" DIC Data

Different strain tensors can be computed from displacement data. A commonly-computed strain tensor in DIC is the Green–Lagrange tensor, whose components in 2D are:

$$E_{xx} = \frac{\partial u}{\partial x} + \frac{1}{2}\left(\left(\frac{\partial u}{\partial x}\right)^2 + \left(\frac{\partial v}{\partial x}\right)^2\right) \tag{5a}$$

$$E_{yy} = \frac{\partial v}{\partial y} + \frac{1}{2}\left(\left(\frac{\partial u}{\partial y}\right)^2 + \left(\frac{\partial v}{\partial y}\right)^2\right) \tag{5b}$$

$$E_{xy} = \frac{1}{2}\left(\frac{\partial u}{\partial y} + \frac{\partial v}{\partial x} + \frac{\partial u}{\partial x}\frac{\partial u}{\partial y} + \frac{\partial v}{\partial x}\frac{\partial v}{\partial y}\right) \tag{5c}$$

where u and v are the displacements along the x and y directions respectively. There are many methods available to compute the spatial gradients in the above equation as mentioned in [38]. Here, we use a polynomial shape function, described in more detail in [34]. The displacements computed at the points of interest using this method are the same as obtained from applying a Savitsky-Golay filter of the same order, but we maintain a polynomial description here in order to obtain the coefficients for the gradients. To prevent redundancy, the spatial gradient calculation method is shown for a general displacement, U^i which can represent either u or v-directions through the i superscript. For a given experimental displacement field, $\boldsymbol{U}^i_{exp}$, we fit a polynomial $\boldsymbol{U}^i_{poly}$ defined by

$$\boldsymbol{U}^i_{poly} = [\boldsymbol{\xi}]\{\boldsymbol{\alpha}^i\}. \tag{6}$$

The function, consisting of a polynomial basis matrix $[\boldsymbol{\xi}]$, and a vector of coefficients $\boldsymbol{\alpha}^i$, is fit to an area defined by the virtual strain gage (VSG) size.

The polynomial basis matrix is of dimension $M \times P$ where M defines the number of points used in the strain calculation through their local coordinates $\boldsymbol{x}$ and $\boldsymbol{y}$, and P describes the number of basis functions used in the polynomial. For this paper we utilize an affine shape function given in equation (7a) whose coefficients consist of rigid displacements u_0, v_0, and partial derivatives in equation (7b) to account for uniform stretching, compression, and shear.

$$[\boldsymbol{\xi}] = \begin{bmatrix} 1 & \boldsymbol{x} & \boldsymbol{y} \end{bmatrix} \tag{7a}$$

$$\boldsymbol{\alpha}^i = \langle U_0^i, \frac{\partial U^i}{\partial x}, \frac{\partial U^i}{\partial y}\rangle \tag{7b}$$

$$(\boldsymbol{\alpha}^*)^i \equiv \min_{\boldsymbol{\alpha}^i}\left(\boldsymbol{U}^i_{poly}(\boldsymbol{\alpha}^i) - \boldsymbol{U}^i_{exp}\right)^T\left(\boldsymbol{U}^i_{poly}(\boldsymbol{\alpha}^i) - \boldsymbol{U}^i_{exp}\right) \tag{8}$$

We solve the least-squares problem in equation (8) to obtain optimized coefficient vectors $(\boldsymbol{\alpha}^*)^i$, which gives us the partial derivatives for the experimental strain.

Direct-levelling of FEA Data

During our FEMU analysis, ϵ_{FEA} is calculated at the DIC grid locations using several degrees of direct-levelling. The flow chart in Fig. 6 provides a visual aid to understanding the multiple different techniques of direct-levelling employed here and how they compare with the "DIC-levelling" presented in [15]. In the figure, we distinguish the different degrees of direct-levelling such as subset, tensor, and strain-levelling and discuss their implementation in the following subsections.

Raw (unlevelled) strains calculated in abaqus

Due to the incremental theories used in commercial FEA software, different measures of strain such as the total (integrated) strain, engineering strain, and logarithmic strain, can be reported. The default strain measurement for our model in ABAQUS is the "logarithmic strain", $\boldsymbol{\epsilon}$, shown in equation (9), where $\mathbf{B}$ is the left Cauchy-Green strain tensor composed of the deformation gradient, $\mathbf{F}$ [41].

$$\boldsymbol{\varepsilon} = \ln(\sqrt{[\mathbf{B}]}) = \ln(\sqrt{[\mathbf{F}] \cdot [\mathbf{F}]^{\mathrm{T}}}) \qquad (9)$$

This data set was interpolated without modification using the triangulation-based cubic scheme in MATLAB from the FE integration points to the DIC grid. In this way, the unlevelled FEA data and synthetic "experimental" DIC data were both on the same grid, so direct subtraction of the strain could occur on a point-by-point basis. This data is referred to "unlevelled" FEA strains.

Tensor-levelled FEA strains

To address the discrepancy between the FEA and DIC strain tensors, we must calculate the same strain tensor for both data sets. Since ABAQUS does not have an option to export the Green–Lagrange strain directly for the simulation we performed, we calculated it using the same polynomial method presented in "Strain Calculations for "Experimental" DIC Data". To largely isolate the effects of the strain tensor from effects of length-scale or spatial resolution, we used a constant VSG size of 0.4 mm for the FEA results; some attenuation of the underlying strain is present (see Fig. 4), but this was the smallest practical VSG size that could be used while containing reasonable amounts of nodal points. We call this set of FEA strains "tensor-levelled", since the FEA and DIC strains were computed using the same strain tensor, but the two data sets still have differing spatial resolution based on the varying DIC VSG size.

Strain-levelled FEA strains

To address the discrepancy of length scale for strain calculations between the FEA and DIC strains, the Green–Lagrange strains were calculated from the FEA displacements using the polynomial shape function method in "Strain Calculations for "Experimental" DIC Data". Importantly, the VSG size was selected to match the different VSG sizes used for the synthetic "experimental" DIC strains. We call this set of FEA strains "strain-levelled" since it used the same strain calculation procedure and thus has the same spatial resolution as the "experimental" DIC strains.

Subset-levelled FEA displacements

Strain attenuation bias is usually much larger than subset shape function attenuation bias, due to the longer length scale of the VSG compared to the subset. However, when the differences in spatial resolution between the FEA and DIC displacements are not negligible, further levelling may be required to obtain an accurate identification. To account for subset shape function attenuation bias, the
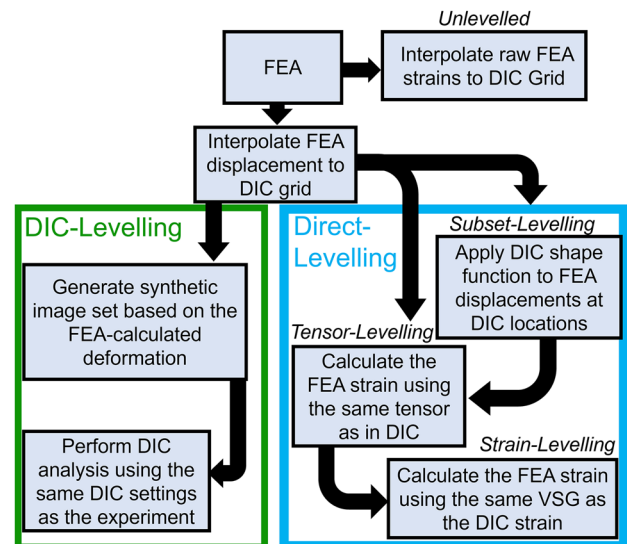

Fig. 6 Flowchart defining the levelling processes. The DIC-levelling process (green box) involves the DIC analysis of synthetic images generated by the FEA data and accounts for both group 1 and group 2 image-induced errors (with the exception of subpixel interpolation bias). Direct-levelling (blue box) accounts for only group 1 errors by applying the DIC filtering biases directly to the FEA nodal displacement data without the generation and correlation of synthetic images

polynomial method in "Strain Calculations for "Experimental" DIC Data" was applied with a square window size of 21 pixels × 21 pixels and an affine shape function, mimicking the effect of the subset in the DIC matching algorithm. These "subset-levelled" displacements $[u_0, v_0]$, are equivalent to what would be obtained by applying a Savitzky-Golay filter of order 1 to the underlying displacements but are obtained here from the first index of $(\boldsymbol{\alpha}^*)^i$ in equation (8). Once the displacements were subset-levelled, the strains were computed as described in "Strain-levelled FEA strains". Thus, this FEA data is both subset-levelled and strain-levelled.

Results and Discussion

Effect of Tensor-Levelling and Strain-Levelling

FEMU using synthetic "experimental" data set 1: Effect of dissimilar strain spatial resolutions

Using the first synthetic "experimental" data taken directly from FEA ("Strain Calculations for "Experimental" DIC Data"), three sets of FEMU calibrations were performed for the 10 VSG sizes. Figure 7 shows the identification results for FEA strains that were either unlevelled, tensor-levelled, or strain-levelled. The cyan markers are from optimizing

the unlevelled (UL) ABAQUS-produced logarithmic strain from equation (9) to the Green–Lagrange strain in equations (5a, 5b, 5c). This data did not account for either different strain tensors (i.e. logarithmic versus Green–Lagrange) or different spatial resolutions (i.e. a FEA element size that is approximately $10\times$ smaller than the smallest DIC VSG size of 0.4 mm). The blue markers represent a tensor-levelled (TL) calibration, where both the FEA strains and the DIC strains were computed using the Green–Lagrange tensor, but at different length-scales (VSG size of 0.4 mm for the

Fig. 7 FEMU calibration results between levelled and unlevelled FEA strain for σ_0, B, and n using synthetic "experimental" data set 1. The calibration results for the unlevelled FEA strains (UL) and the tensor-levelled strains (TL) were inaccurate, with generally growing levels of error as the VSG size increased. The results for the strain-levelled FEA strains (SL) were accurate to nearly machine precision, showing that the strain-levelling process results in an accurate and unique identification via FEMU. For a VSG size of 0.4 mm, there is no distinction between methods used for the blue and red markers.

tensor-levelled FEA strains and varying VSG sizes for the synthetic DIC strains). At the VSG size of 0.8 mm, the error in the tensor-levelled results as compared to the unlevelled calibration was reduced from 8.54% to -0.29% for σ_0, 9.38% to 0.84% for B, and -4.40% to 2.29% for n. While tensor-levelling reduced the parameter errors, both results were inaccurate with significant biases depending on the VSG size.

For the last calibration, the strain-levelled (SL) FEA strains were computed using the same tensor and VSG size as was used in the DIC strain computation. In this way, both the FEA and DIC strains had the same filtering and same spatial resolution. The strain-levelled calibrations (red markers) were all successful in acquiring the correct parameters with near machine-precision errors. The errors for all three data sets for the more reasonable VSG of 0.8 mm, as well as the maximum error using the VSG of 4.0 mm, are quantified in Table S2 in the supplementary information.

We have shown using synthetic "experimental" data taken directly from FEA data (no DIC images) that if the differing spatial resolution of FEA and synthetic DIC data is not taken into account, inaccurate model parameters may be identified that moreover depend on user-defined DIC settings such as VSG size. This result highlights the effect of group 1 filtering errors. By levelling the FEA data first, however, a unique and exact set of parameters can be found. This accuracy remained true even with the unreasonably large VSG of 4.0 mm, suggesting uniqueness of the solution under low noise despite heavy filtering of the underlying strain data.

FEMU using synthetic "experimental" data set 2: Effect of group 2 image errors

FEMU was also performed using the second synthetic "experimental" data set, to test the accuracy of direct-levelling using synthetic DIC images so errors related to subset shape function attenuation bias, digital images (group 2 errors), and noise can be evaluated. The synthetic images were processed through either MatchID with a quadratic subset shape function and bicubic spline interpolant or in VIC2D with an affine shape function and 8-tap interpolant. Since both DIC data sets yielded similar FEMU identification results, only the MatchID results are shown for brevity here. The reader is referred to Tables S5, S6 in the supplementary information to see the identification results using DIC data analyzed in VIC2D.

Building from the results presented in "FEMU using synthetic "experimental" data set 1: Effect of dissimilar strain spatial resolutions" that addressed group 1 strain-filtering errors, we start with the noise-free image set to analyze the effect of group 2 errors related to the image intensity map and its interpolation. Figure 8 shows that the unlevelled (UL) and tensor-levelled (TL) calibrations performed poorly and had similar identification results as the FEMU identification
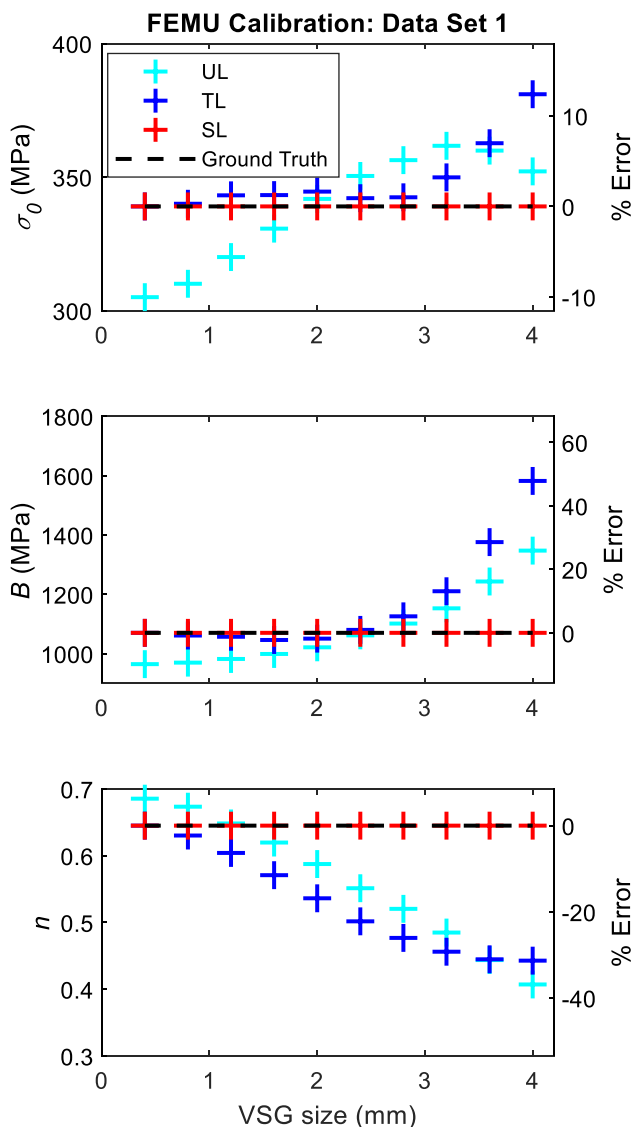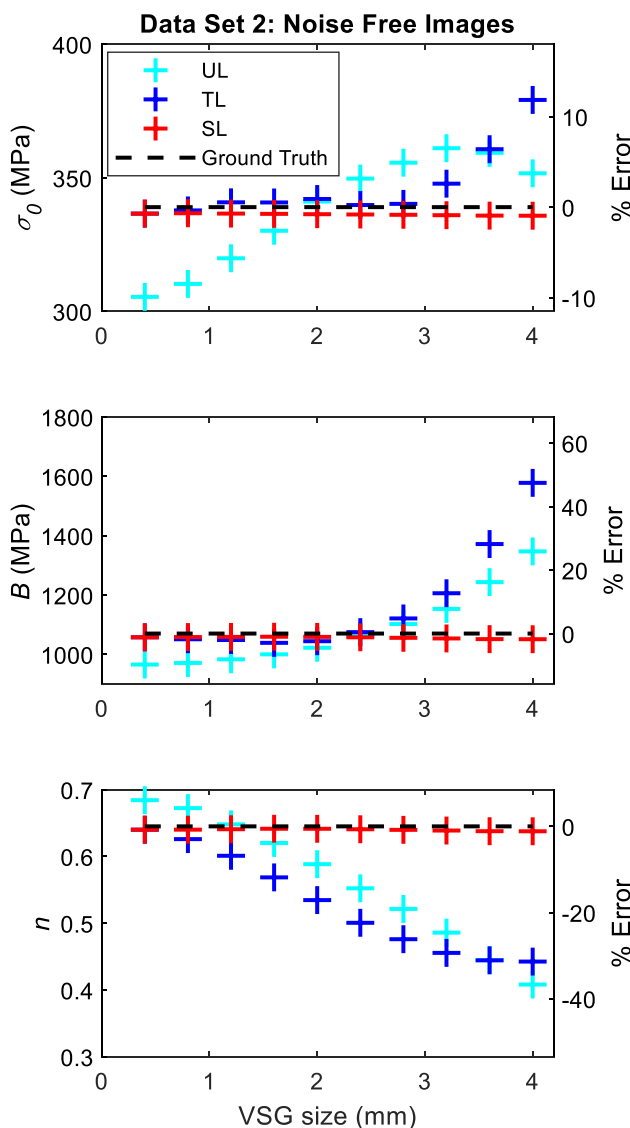
Fig. 8 Found parameters for the FEMU calibration between the strain computed using the MatchID-measured deformation of the synthetic images and the levelled and unlevelled FEA strain. The strain-levelled calibrations performed well for all VSG sizes despite errors introduced from the images

using data set 1 (no synthetic DIC images) shown in Fig. 7. Thus, the identification error in the unlevelled and tensor-levelled results is attributed to the dissimilarity of the strain tensors and disparity in the spatial resolution between the FEA and synthetic "experimental" data and not the image errors themselves.

In contrast, the strain-levelled (SL) calibrations were all much more successful in acquiring the correct parameters, regardless of the VSG size. For the noise free images, parameters were calibrated with errors of 0.68% for σ_0, 1.10% for B, and 0.76% for n for the 0.8 mm VSG. Results for all three levelling methods are reported in the first three columns of

Tables S3-S6 in the supplementary information for VSG sizes of 0.8 mm and 4.0 mm. The error contribution from the image (group 2) is smaller by a factor of 10 compared to the error contribution from differing strain spatial resolution (group 1). Thus, the group 2 biases introduced by the images, namely image discretization errors [4, 6], pattern induced bias [4, 5], and subpixel interpolation bias from the bicubic spline interpolant [2, 5], have negligible influence on model calibration. This result suggests that direct-levelling, which bypasses the synthetic image generation and DIC analysis steps, can provide a more computationally-efficient route to addressing differing spatial resolutions compared to the full DIC-levelling process.

We have demonstrated the importance of levelling for FEMU calibration and have shown that the error contribution from the images (group 2) have a smaller contribution in the bias compared to the mismatch in filtering (group 1). Further, we showed that an accurate set of material model parameters can be found despite the use of an unreasonably large VSG in the DIC analysis. We build on our investigation by exploring how the DIC displacement shape function affects the accuracy of the calibration.

FEMU using synthetic "experimental" data set 2: Effect of dissimilar displacement spatial resolutions

As already briefly mentioned, the spatial resolution of a measurement, be it displacement or strain, is dependent in part on the shape function used. The results in "FEMU using synthetic "experimental" data set 1: Effect of dissimilar strain spatial resolutions" and "FEMU using synthetic "experimental" data set 2: Effect of group 2 image errors" focus on the effect of strain attenuation bias. Here, the smaller, but still noticeable, effect of subset shape function attenuation bias is discussed.

Figure 9 shows two vertical line-cuts from the noise-free images of the E_{yy} and E_{xy} strains using a VSG size of 0.8 mm. The strains shown by the red and black lines were derived from DIC displacements measured using either a quadratic or affine subset shape function, respectively. The E_{yy} strain shown in Fig. 9(a) was sampled from near the center of the specimen like in Figs. 4, 5, and the E_{xy} strain shown in Fig. 9(b) was sampled closer to the edge of the neck where the shear strains are non-zero. The E_{xx} strains were omitted for brevity, but all three strain components showed only a minor difference in the peak height caused by subset shape function attenuation bias from the lower order shape function.

Since there was not an obvious difference in the measured strain for the two subset shape functions, it is reasonable to expect that there would be a negligible difference in the calibration results. Surprisingly, though, Fig. 10 shows that the resulting calibration using the affine shape function (black markers) performs unfavorably compared to the quadratic
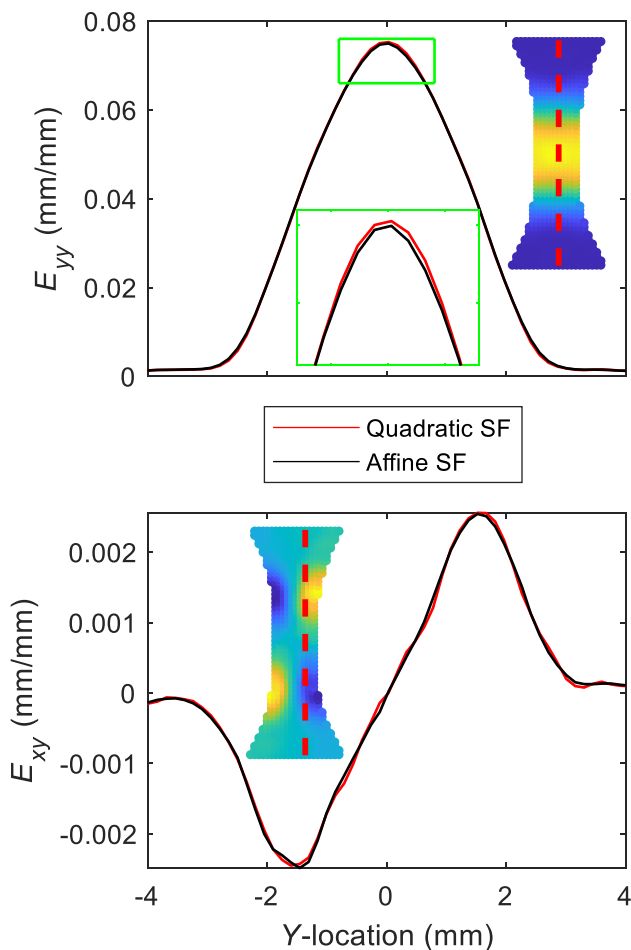
Fig. 9 Vertical line-cuts of the E_{yy} and E_{xy} strain using a VSG size of 0.8 mm and either a quadratic or affine subset shape function in MatchID. Peak heights are nearly identical for both shape functions, indicating negligible subset shape function attenuation bias
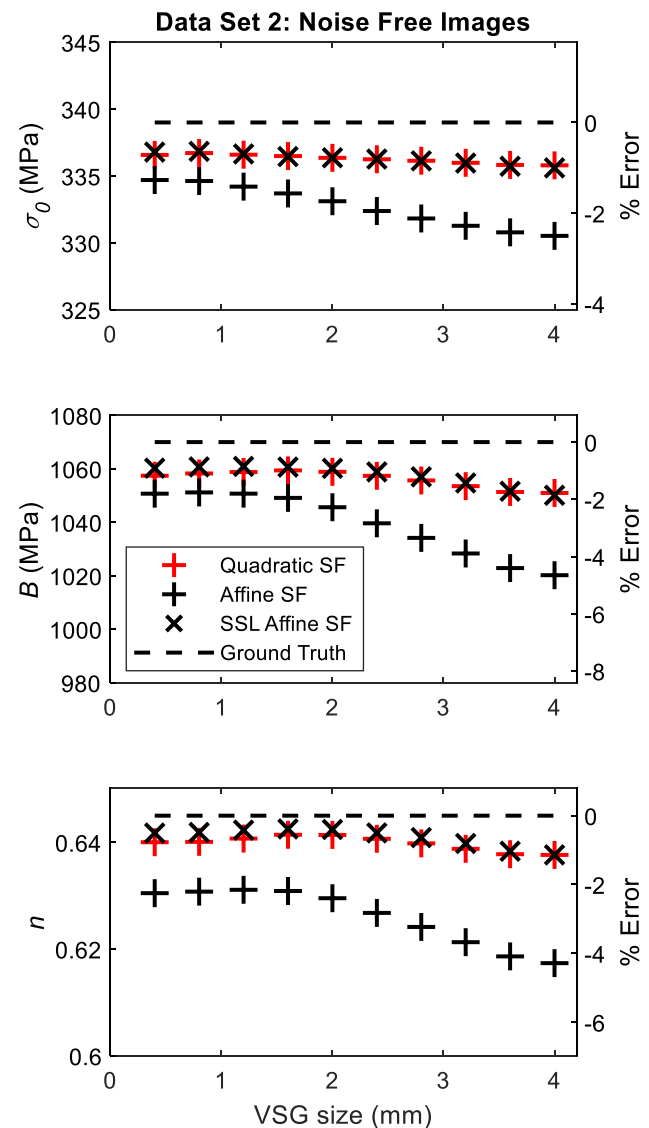

Fig. 10 Identified parameters for the FEMU calibration using strain levelling (SL) and a quadratic shape function (red markers), an affine shape function (black markers) and an affine shape function with subset levelling performed on the FEA displacement before the strain levelling (black markers). MatchID was the DIC software used here to measure the displacements used to compute the strain

results (red markers) when the FEA displacements were not subset-levelled before strains were calculated.

To correct for the minor shape function attenuation bias, the FEA displacements were subset-levelled following the method described in "Subset-levelled FEA displacements". Then, the strains were calculated as described in "Strain-levelled FEA strains". Thus, the FEA data were both subset-levelled (SSL) and strain-levelled. These results are represented by the black markers in Fig. 10 and show a marked decrease in errors from 1.29% to 0.64% for σ_0, 1.76% to 0.87% for B, and 2.21% to 0.49% for n in the noise-free images.

These results confirm that the strain attenuation from the relatively large VSG length scale is the dominating factor in the spatial resolution disparity. However, the effect of subset shape function attenuation is a second order effect that may add some error to calibration results, especially if an affine subset shape function is used. We showed that this error can be corrected by subset-levelling the FEA

displacements before calculation of the strain tensor. Performing this subset-levelling yielded results similar to those when using a higher order shape function e.g. quadratic. The more complicated subset-levelling comes with additional computational cost, increasing the average solve time from approximately 16 min to around 23 min for a calibration with around 6–7 FEMU iterations. It is our opinion that this is only a modest increase in computation time, and thus we recommend this procedure to obtain more accurate identification results.

FEMU using synthetic "experimental" data set 2: Effect of image interpolant quality and image noise

In "FEMU using synthetic "experimental" data set 2: Effect of dissimilar displacement spatial resolutions", the DIC images were processed in MatchID, as VIC2D is limited to the lower order affine shape function. However, as we showed in Fig. 10, by subset-levelling, lower order shape functions can be used in the DIC analysis to obtain FEMU identification results commensurate with the use of higher order shape functions in DIC. Therefore, we now perform FEMU using VIC2D along with its higher order 8-tap interpolant to assess the effect of image interpolation, and later image noise, on the identification results.

Figure 11 first presents calibration results for the noise-free images (left column) with an affine shape function without subset-levelling (black markers). Compared to the corresponding results from MatchID in Fig. 10, the errors are reduced slightly (see Tables S4 and S5 in the supplementary information). This improvement is attributed to a better image intensity interpolant in VIC2D. When the FEA data is both subset-levelled and strain-leveled (black markers), the calibration results with noise-free images have high accuracy for all VSG sizes, with an error of -0.06% for σ_0, -0.29% for B, and -0.23% for n using the 0.8 mm VSG. This level of accuracy is the result of a smooth noise-free DIC pattern in conjunction with a high-order interpolant. Therefore, this level of accuracy might not be achieved in a real experiment. However, we use these small errors to serve as a basis on which we discuss the error solely due to image noise, and its relation in magnitude to group 1 errors.

The calibration results using the noisy images are shown in the right column of Fig. 11, again for FEA data that was either only strain-levelled (black markers) or subset and strain-levelled (black markers). For the subset- and strain-levelled data, the final parameters were calibrated with errors around 1% for all parameters and VSG sizes (see Table S5 in the supplementary information). By visually comparing the FEMU results from the noise free images to those of the noisy images, it can be concluded that the bias due to undermatched subset (and by extension, strain) shape functions is more of a detriment to accuracy than image noise.

In summary, FEMU identifications using strain-levelled (and subset- and strain-levelled for lower order DIC shape functions) FEA data performed well with parameter errors around 1% or less for both the noise free and noisy images.

FEMU using synthetic "experimental" data set 2: Effect of step size

The importance of DIC step size for model calibration using full-field data has recently been recognized [1], where previous works optimized both specimen geometry and DIC settings in either a two-step [42] or one-step [43] process and

found that a step size of 1 pixel was superior. Here, the effect of step size on material model parameter identification using noisy images was briefly investigated by reducing it from the 7 pixels used previously to 2 pixels. Figure 12 shows the calibration results from VIC2D with an affine subset shape function, where the FEA data was subset and strain-levelled. The 7-pixel step size results are repeated from Fig. 11 (black markers), with the 2-pixel results (red □ markers) overlaid. The identified parameters had essentially the same accuracy, despite the approximately 10X increase of points used in the strain calculation for each VSG size with the 2-pixel step size. Thus, for this exemplar test, the step size did not have a noticeable impact on the model calibration.

Identification Error Due to Incorrect FE Model to DIC Registration

In the previous sections, the location of the DIC points was known exactly in relation to the FE model. However, in an experiment, coordinate alignment may be non-trivial due to factors such as limited spatial resolution, specimen manufacturing errors [15], precise marking of fiducials on the specimen and identification of fiducials in the DIC images, lens distortion, or the lack of software to perform this alignment. Misalignment from the FE model to the DIC grid could be the dominant error in the strain comparison between the experimental and FEA data, as the authors in [15] noted for FE model validation. However, the relation between the magnitude of misalignment to error in the identification is less clear. While the alignment problem could be reduced by building the FE model using topology measurements gathered through stereo-DIC or industry standard quality-control tools such as a coordinate-measuring machine (CMM), this step adds additional complexity to the simulation workflow and is not typically done. For example, DIC can only capture a single side of the geometry without data stitching, and a CMM can only capture points in contact with the probe making accurate shape measurement timely [44].

Here we intentionally induced a misalignment by rigidly shifting the FE grid with respect to the DIC in 1-pixel increments in the vertical (Y), diagonal (45 degrees), or horizontal (X) direction. The calibration was then repeated using the noise-free images of the synthetic DIC data set 2, with an affine shape function in VIC2D, a step size of 7 pixels, and subset and strain-levelled FEA data. The registration error created a bias in the calibration results that was consistent for all VSG sizes, so we report here only the results for the 0.8 mm VSG.

Figure 13 presents the calibration results as a function of the magnitude of misalignment. Additionally, the results for the corresponding perfectly aligned case (Fig. 11, black markers, VSG size of 0.8 mm) are displayed for comparison at the zero position on the "Alignment Error" axis. For
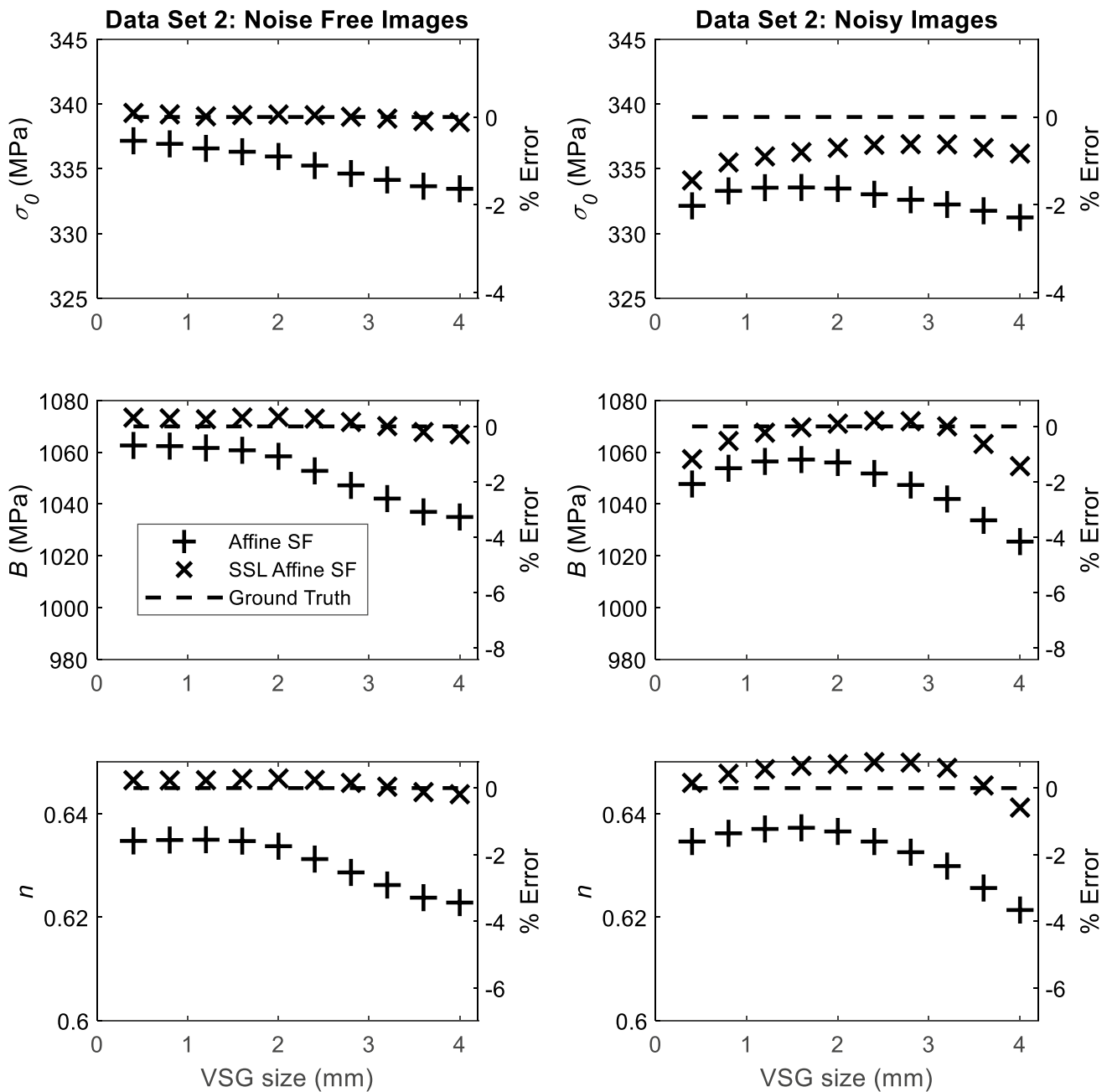
Fig. 11 Identified parameters for the FEMU calibration using strain levelling (SL) and an affine shape function for the displacement measured in VIC2D. The calibration results are shown above (black markers) for both the noise free images and noisy image data sets. The calibration was repeated, this time with subset levelling of the FEA displacement before the strain levelling (black markers). The results show that the error due to noise and intensity interpolation and noise is small compared to the bias due to the undermatching of the affine shape function to the underlying displacement

all misalignment directions, the identified parameter value diverged from the aligned value as a function of the magnitude of misalignment. The effect of misalignment was most pronounced for the hardening exponent, n, followed by the yield stress, σ_0 and hardening rate, B. Due to the loading, most of the strain gradients occur along the Y-direction, resulting in more error due to vertical misalignment than horizontal or diagonal misalignment.

For a small amount of misalignment that would be commensurate with a real experiment, e.g. 3–4 pixels, the difference between the identified parameter values with and without misalignment is less than 1% for all parameters and directions of misalignment. Therefore, the error due to misalignment (see Table S7 in the supplementary information) is smaller than that caused by the filtering of an affine subset
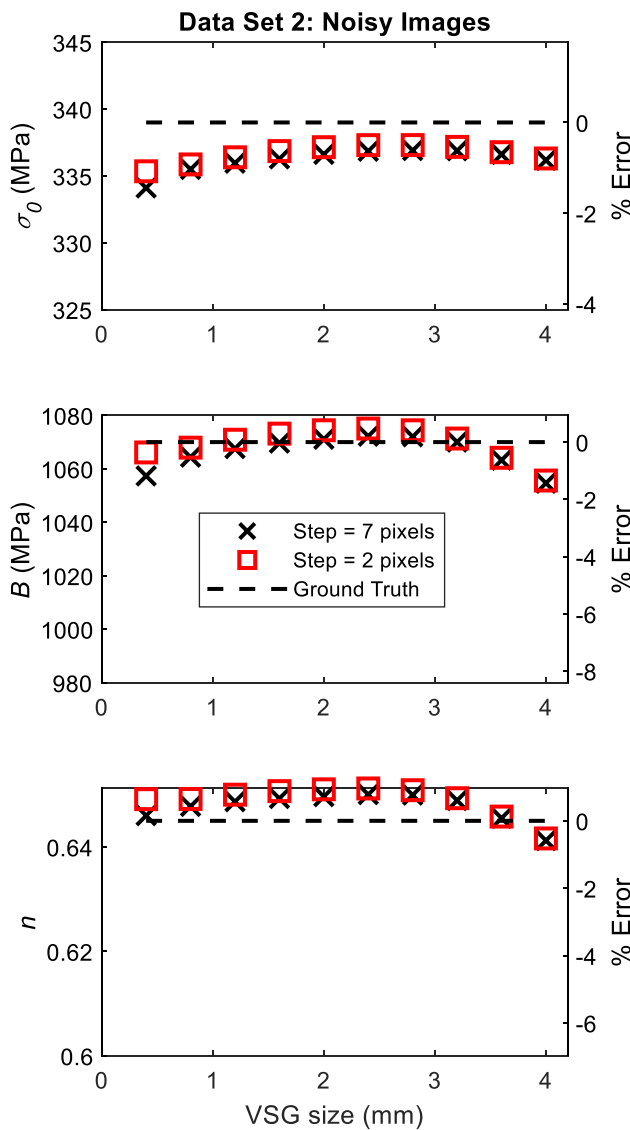
Fig. 12 Identified parameters for the FEMU calibration using subset and strain-levelling with either a step size of 7 pixels (black markers) or 2 pixels (red □ markers) in VIC2D. The use of smoother DIC-measured strains through decreasing the step size to 2 pixels resulted in negligible change in the identification results
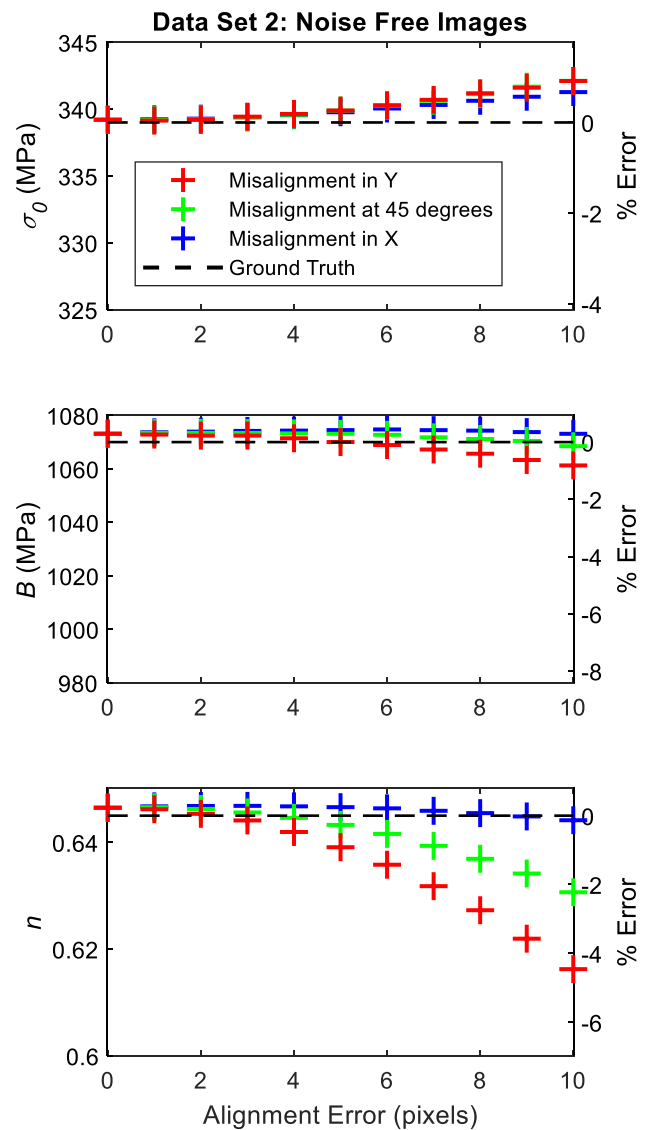
Fig. 13 Identified parameters as a function of FE model-to-DIC misalignment using subset and strain-levelled FE strain and VIC2D measured strains with an affine shape function and a step size of 7 pixels. The Y-direction misalignment results in larger errors since most of the strain gradients are oriented along the vertical axis

shape function and much larger than that caused by the filtering of the VSG (see Table S3).

Conclusions

As material models become more complex, full-field data from heterogeneous specimens can provide rich information for model calibration. However, the adoption of full-field deformation measurements such as from DIC into inverse parameter calibration processes such as FEMU may introduce problems of data (in)compatibility that can corrupt identification.

To address this problem, we propose to "level" the FEA data so that it has the same filtering and spatial resolution as the experimental DIC data, before the FEMU cost function is computed. Complete DIC-levelling involves generating synthetic DIC images based on the FEA and processing them in the DIC software using the same user-defined settings (e.g. VSG size) as the experimental images. We investigated direct-levelling as a computationally more efficient method to bypass the image generation and correlation steps. We evaluated three degrees of direct-levelling that successively account for more of the group 1 errors: 1) tensor-levelling, where FEA strains are computed using the same tensor as experimental DIC strains, but may still

have a smaller length scale; 2) strain-levelling, where FEA strains are computed using the same VSG size as the experimental DIC strains, but using the unfiltered FEA displacements; and 3) subset and strain-levelling, where FEA displacements are first filtered with the DIC subset shape function, and then strains are computed with the same VSG size.

To demonstrate the necessity and efficacy of direct-levelling, we generated a ground-truth FEA with an elasto-plastic material model based on 304L stainless steel. Then, we created two sets of synthetic "experimental" DIC data based on the FEA: the first set used strains computed directly from the FEA nodal displacements, which accounted for group 1 spatial resolution and filtering errors, and the second set used synthetic DIC images, which additionally included group 2 image errors. Using these synthetic "experimental" data sets (with a known ground-truth reference solution), we showed that levelling of the finite element model results, so the FEA and DIC data both have the same filtering and spatial resolution, is necessary for an accurate calibration via FEMU. Key findings are that:

- Unlevelled FEA strain data (i.e. logarithmic strains output directly from ABAQUS with the FE mesh element size governing the spatial resolution) caused large errors of up to 10% for reasonable VSG sizes in the FEMU parameter identification process.
- Tensor-levelling the FEA strains (i.e. computing Green–Lagrange strain from the FEA displacements to match the tensor of the "experimental" DIC strains) reduced the error somewhat, but still resulted in parameter errors up to 3%.
- Strain-levelling the FEA data (i.e. using the same VSG size as the "experimental" DIC strains) resulted in zero error (to machine precision) for all VSG sizes when using the first set of synthetic "experimental" data. Critically, the parameter results did not depend on user-defined DIC settings and did not require converged experimental strain measurements.
- For noise-free images, image-induced errors (e.g. pattern-induced bias, intensity discretization, and subpixel interpolation bias) in the DIC results were negligible in the calibration process, resulting in identification errors less than 1% on average–well below the biases from subset shape function and strain attenuation bias.
- Errors due to image noise were also small, approximately 1–3% error for the smallest VSG size and best direct-levelling settings.
- Identification errors using an affine subset shape function were around 1 percentage point higher than the identification results using a quadratic subset shape function. However, subset-levelling with affine shape

functions addressed this issue and gave results commensurate with quadratic shape functions.
- The 8-tap image intensity interpolant performed better than the bicubic spline interpolant, reducing parameter errors from approximately 3% to 1% for noisy images.
- Parameter errors were insensitive to step size, with both 7 pixels and 2 pixels producing equivalent results.
- Small amounts of misalignment between the FE model and the DIC grid (4 pixels) did not significantly affect parameter results, while larger amounts (10 pixels) increased parameter error by up to 4 percentage points.

The above conclusions are specific to the case study used here (i.e., specimen geometry, FE mesh size, and DIC hardware and software settings) and are not necessarily generalizable to all experimental setups. However, when measuring deformation using DIC, it is difficult to know when the strain is sufficiently resolved, particularly when deformation is highly localized such as in the neck region of a tensile bar or near strain concentrators like holes or notches. The power of this direct-levelling technique is that a converged DIC result is no longer required to obtain accurate material model calibrations. Direct-levelling improves the accuracy of FEMU and the concepts could be applied to other inverse methods that utilize full-field measurements. Since the topic of DIC-levelling is still new, we offer a simple approach that can be applied using local DIC without the need for generating synthetic images, making direct-levelling easier and more efficient to incorporate into the FEMU workflow.

to these results of federally sponsored research in accordance with the DOE Public Access Plan https://www.energy.gov/downloads/doe-public-access-plan.

Declarations

Conflict of Interest The authors declare that they have no conflict of interest.

References

1. Pierron F, Grédiac M (2021) Towards material testing 2.0. A review of test design for identification of constitutive parameters from full-field measurements." Strain 57(1):e12370. https://doi.org/10.1111/str.12370

2. Schreier HW, Sutton MA (2002) Systematic errors in digital image correlation due to undermatched subset shape functions. Exp Mech 42(3):303–310. https://doi.org/10.1007/BF02410987

3. Grédiac M, Blaysat B, Sur F (2017) Critical comparison of some metrological parameters characterizing local digital image correlation and grid method. Exp Mech 57:871–903. https://doi.org/10.1007/s11340-017-0279-x

4. Fayad SS, Seidl DT, Reu PL (2020) Spatial DIC errors due to pattern-induced bias and grey level discretization. Exp Mech 60:249–263. https://doi.org/10.1007/s11340-019-00553-9

5. Sur F, Blaysat B, Grédiac M (2020) On biases in displacement estimation for image registration, with a focus on photomechanics. J Math Imaging Vis 63:777–806. https://doi.org/10.1007/s10851-021-01032-4

6. Zhao B, Surrel Y (1997) Effect of quantization error on the computed phase of phase-shifting measurements. Appl Opt 36(10):2070–2075. https://doi.org/10.1111/j.1475-1305.2008.00592.x

7. Schreier HW, Braasch JR, Sutton MA (2000) Systematic errors in digital image correlation caused by intensity interpolation. Opt Eng 39(11):2915–2922. https://doi.org/10.1117/1.1314593

8. Wang YQ et al (2009) Quantitative error assessment in pattern matching: Effects of intensity pattern noise, interpolation, strain and image contrast on motion measurements. Strain 45(2):160–178

9. Lyons JS, Liu J, Sutton MA (1996) High-temperature deformation measurements using digital-image correlation. Exp Mech 36(1):64–70. https://doi.org/10.1007/BF02328699

10. Delmas A et al (2013) Shape distortions induced by convective effect on hot object in visible, near infrared and infrared bands. Exp Fluids 54(4):1–16. https://doi.org/10.1007/s00348-012-1452-8

11. Jones EMC, Reu PL (2018) Distortion of digital image correlation (DIC) displacements and strains from heat waves. Exp Mech 58:1133–1156. https://doi.org/10.1007/s11340-017-0354-3

12. Lecompte D et al (2006) Quality assessment of speckle patterns for digital image correlation. Opt Lasers Eng 44(11):1132–1145. https://doi.org/10.1016/j.optlaseng.2005.10.004

13. Reu PL et al (2018) DIC challenge: Developing images and guidelines for evaluating accuracy and resolution of 2D analyses. Exp Mech 58:1067–1099. https://doi.org/10.1007/s11340-017-0349-0

14. Reu PL et al (2021) DIC Challenge 2.0: Developing images and guidelines for evaluating accuracy and resolution of 2D analyses focus on the metrological efficiency indicator. Exp Mech 62:639–654. https://doi.org/10.1007/s11340-021-00806-6

15. Lava P, Jones EMC, Wittevrongel L, Pierron F (2020) Validation of finite-element models using full-field experimental data: Levelling finite-element analysis data through a digital image correlation engine. Strain 56(4):e12350. https://doi.org/10.1111/str.12350

16. MatchID Analysis Packages. https://www.matchid.eu/en/solutions-overview/software/analysis-packages

17. Gothivarekar S et al (2020) Advanced FE model validation of cold-forming process using DIC: Air bending of high strength steel. Int J Mat Form 13(3):409–421. https://doi.org/10.1007/s12289-020-01536-1

18. Jones EMC et al (2021) Anisotropic plasticity model forms for extruded Al 7079: Part II, validation. Int J Solids Struct 213:148–166. https://doi.org/10.1016/j.ijsolstr.2020.11.031

19. Guildenbecher DR et al (2022) 3D optical diagnostics for explosively driven deformation and fragmentation. Int J Impact Eng 162:104142. https://doi.org/10.1016/j.ijimpeng.2021.104142

20. Zhang Y, Andrade-Campos A, Coppieters S (2022) Identification of Anisotropic Yield Functions Using FEMU and an Information-Rich Tensile Specimen. Key Eng Mater 926. Trans Tech Publications Ltd. https://doi.org/10.4028/p-m5q583

21. Zhang H et al (2019) Inverse identification of the post-necking work hardening behaviour of thick HSS through full-field strain measurements during diffuse necking. Mech Mater 129:361–374. https://doi.org/10.1016/j.mechmat.2018.12.014

22. Wang Y et al (2016) Anisotropic yield surface identification of sheet metal through stereo finite element model updating. J Strain Anal Eng Des 51(8): 598–611. https://doi.org/10.1177/2F0309324716666437

23. Mathieu F, Leclerc H, Hild F (2015) Estimation of elastoplastic parameters via weighted FEMU and integrated-DIC. Exp Mech 55:105–119. https://doi.org/10.1007/s11340-014-9888-9

24. Martins JMP, Andrade-Campos A, Thuillier S (2018) Comparison of inverse identification strategies for constitutive mechanical models using full-field measurements. Int J Mech Sci 145:330–345. https://doi.org/10.1016/j.ijmecsci.2018.07.013

25. Lecompte D et al (2007) Mixed numerical–experimental technique for orthotropic parameter identification using biaxial tensile tests on cruciform specimens. Int J Solids Struct 44(5):1643–1656. https://doi.org/10.1016/j.ijsolstr.2006.06.050

26. Rossi M, Pierron F (2012) On the use of simulated experiments in designing tests for material characterization from full-field measurements. Int J Solids Struct 49(3–4):420–435. https://doi.org/10.1016/j.ijsolstr.2011.09.025

27. Wang P, Pierron F, Thomsen OT (2013) Identification of material parameters of PVC foams using digital image correlation and the virtual fields method. Exp Mech 53(6):1001–1015. https://doi.org/10.1007/s11340-012-9703-4

28. Rossi M, Lava P, Pierron F, Sasso D (2015) Effect of DIC spatial resolution, noise and interpolation error on identification results with the VFM. Strain 51(3):206–222. https://doi.org/10.1111/str.12134

29. Jones EMC, Karlson KN, Reu PL (2019) Investigation of assumptions and approximations in the virtual fields method for a viscoplastic material model. Strain 55(4):e12309. https://doi.org/10.1111/str.12309

30. Zhang Y et al (2022) Enhancing the information-richness of sheet metal specimens for inverse identification of plastic anisotropy through strain fields. Int J Mech Sci 214:106891. https://doi.org/10.1016/j.ijmecsci.2021.106891

31. Dufour JE et al (2015) CAD-based displacement measurements with stereo-DIC. Exp Mech 55:1657–1668. https://doi.org/10.1007/s11340-015-0065-6

32. Dubreuil L et al (2016) Mesh-based shape measurements with stereocorrelation. Exp Mech 56:1231–1242. https://doi.org/10.1007/s11340-016-0158-x

33. Vieira RB, Lambros J (2021) Machine learning neural-network predictions for grain-boundary strain accumulation in a

polycrystalline metal. Exp Mech 61:627–639. https://doi.org/10.1007/s11340-020-00687-1

34. Pan B, Xie H, Guo Z, Hua T (2007) Full-field strain measurement using a two-dimensional Savitzky-Golay digital differentiator in digital image correlation. Opt Eng 46(3):033601. https://doi.org/10.1117/1.2714926

35. Sur F, Blaysat B, Grédiac M (2018) Rendering deformed speckle images with a Boolean model. J Math Imaging Vis 60(5):634–650. https://doi.org/10.1007/s10851-017-0779-4

36. Bornert M et al (2017) Shortcut in DIC error assessment induced by image interpolation used for subpixel shifting. Opt Lasers Eng 91:124–133. https://doi.org/10.1016/j.optlaseng.2016.11.014

37. Reu PL (2011) Experimental and Numerical Methods for Exact Subpixel Shifting. Exp Mech 51:443–452. https://doi.org/10.1007/s11340-010-9417-4

38. Jones EMC, Iadicola MA (Eds.) (2018) A good practices guide for digital image correlation. Int Digit Image Corr Soc. https://doi.org/10.32720/idics/gpg.ed1

39. Reu PL (2015) Virtual strain gage size study. Exp Tech 39(5):1–3. https://doi.org/10.1016/j.ymssp.2016.02.006

40. Papazafeiropoulos G, Muñiz-Calvente M, Martínez-Pañeda E (2017) Abaqus2Matlab: a suitable tool for finite element post-processing. Adv Eng Softw 105:9–16. https://doi.org/10.1016/j.advengsoft.2017.01.006

41. Smith M (2009) / ABAQUS/Standard User's Manual Sec. 1.4.2, Version 6.9., Providence, RI : Dassault Systèmes Simulia Corp

42. Gu X, Pierron F (2016) Towards the design of a new standard for composite stiffness identification. Composites Part A: Appl Sci Manuf 91:448–460. https://doi.org/10.1016/j.compositesa.2016.03.026

43. Gu X, Pierron F (2016) Full optimization of the T-shaped tensile test using genetic algorithm. Internal report, University of Southampton, UK. http://www.camfit.fr/documents/Progress_report_Xuesen_Tshape.pdf

44. Kaszynski AA, Beck JA, Brown JM (2014) Automated finite element model mesh updating scheme applicable to mistuning analysis. Turbo Expo: Power for Land, Sea, and Air. Vol. 45776. Am Soc Mech Eng. https://doi.org/10.1115/GT2014-26925